Supporting Information:

Hydrogen-bonding-enhanced green wearable sensors with high generation performance and low Young's modulus

Caixia Gao, Wangshu Tong*, Runfeng Yu, Songling Liu, Yihe Zhang*

Engineering Research Center of Ministry of Education for Geological Carbon Storage and Low

Carbon Utilization of Resources, Beijing Key Laboratory of Materials Utilization of Nonmetallic

Minerals and Solid Wastes, National Laboratory of Mineral Materials, School of Materials Science

and Technology, China University of Geosciences (Beijing), 100083, China

1. Experimental methods

1.1 Materials

CS (deacetylated ≥ 95%), glycerin (AR, 99%), diatomite (MW 60.08) and acetic acid (AR, 99.5%) were procured from Macklin. Deionized water, aluminum foil, double-faced adhesive tape, FEP (thickness 0.15 mm), and magnesium (Mg) foil (thickness 0.05 mm) were obtained from a native shop.

1.2 Preparation of the CS-glycerin-diatomite composite film

CS-glycerin-diatomite composite films were fabricated by casting method. The CS solution was obtained by adding 0.3 g of CS powder to 10 ml of acetic acid solution (2% v/v). Subsequently, the solution was stirred continuously in an oil bath at 30 °C for 6 h to obtain a viscous, yellowish transparent CS solution. Then, different contents of glycerin solution and diatomite were added to the CS solution and stirred continuously for 3 hours in an oil bath at 30 °C to obtain a CS-glycerin-diatomite mixture, the solution was then left to degas for 5 h until no air bubbles were present. The homogeneous CS-glycerin-diatomite solution obtained was added dropwise to a petri dish and then dried at 60 °C for 4 hours to obtain the CS-glycerin-diatomite composite film.

1.3 Fabrication of CS-glycerin-diatomite/FEP based TENG

The CS-glycerin-diatomite/FEP-based TENG comprising CS-glycerin-diatomite composite film and FEP film was designed to realize a vertical contact-separation mode

1 TENG. The CS-glycerin-diatomite composite film served as a positive friction layer,

2 while the FEP film served as a negative friction layer. The Mg foil acted as an electrode.

3 The total area of the films was 1.5 × 1.5 cm.

1.4 Measurement and characterization

5 The morphology and structure of CS-glycerin-diatomite composite film was

6 characterized using field emission SEM (Zeiss Gemini 300 scanning electron

7 microscope). A Fourier-transform infrared (FTIR) spectrometer (Frontier, Perkin

8 Elmer, USA) was used to measure the infrared absorption spectra of samples and

9 analyze its characteristics. The output performance of the CS-glycerin-diatomite

10 composite film/FEP TENG was tested using a galvanometer (Keithley Model 6517B).

11 A closed-loop linear motor system was used to apply force and a pressure control

12 system was used to implement the contact and separation process. The stress-strain

13 curves were measured on a universal testing machine (Chengde Sheng Testing

14 Equipment Co., Ltd China). By fitting the stress-strain curve linearly, the Young's

15 modulus of CS-glycerol-diatomite was determined (The Young's modulus was

16 calculated by taking the first 5% of the stress-strain curve)[1-5]. The values of Young's

17 modulus were all calculated at a stress-strain measurement rate of 50 mm/min (The

18 dimensions of the CS-glycerol-diatomite film were 20 mm in length and 10 mm in

19 width, and the thickness of the film was 0.24 mm), and three tests were performed and

20 averaged. A strain of Escherichia coli (*E. coli*) was cultured overnight in Luria-Bertani

21 medium, and 10 μL was spread on the plate. The strain was grown for 16 h at 37°C in

22 an incubator. The test film (CS-glycerin-diatomite composite film) was cut into circles

23 and placed on the plates. After 24 h of incubation at 37 °C, size of clear zone that might

24 appear on the plate was checked, and the incubation of the microbial species was

25 recorded.

1.5 Vitro biodegradable test of the CS-glycerin-diatomite composite film

27 The dimensions of CS-glycerin-diatomite composite film were fixed at 1 × 1 cm.

28 The CS-glycerin-diatomite composite film was placed in outdoor soil and photographed

29 at various times to observe their degradation process until complete degradation.

30

2. EDS data for chitosan films and chitosan-glycerin-diatomite composite films

Element	Weight (%)
Si	0.44
O	99.56

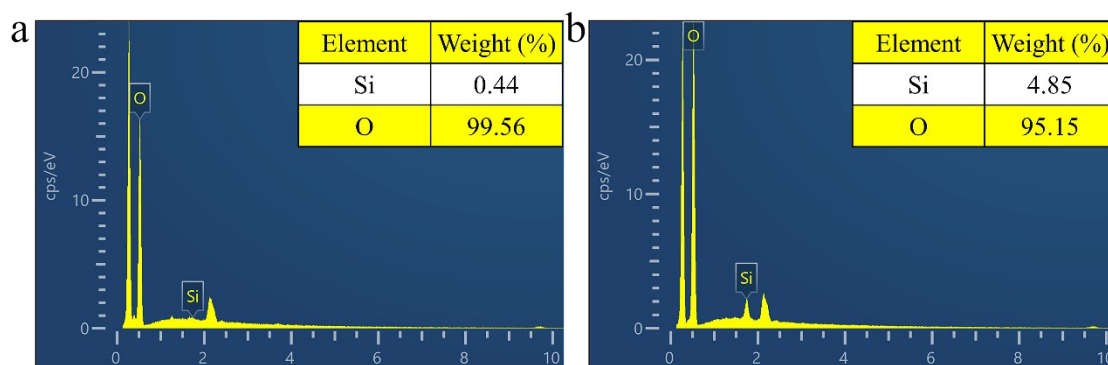| Element	Weight (%)
Si	4.85
O	95.15

Figure S1 (a) EDS data for chitosan films. (b) EDS data for chitosan-glycerin-diatomite composite films.

3. The Young's modulus

The Young's modulus of the CS film is 13.706 KPa and that of the CS-glycerol-diatomite film is 0.3191 KPa. The values of Young's modulus were all calculated at a stress-strain measurement rate of 50 mm/min, three tests were conducted and averaged with a standard deviation of 0.03. The CS-glycerol-diatomite composite film has a lower Young's modulus due to the addition of glycerol and diatomite, which introduces more hydroxyl groups to disrupt the internal interactions of the CS resulting in greater deformation in friction process. On the contrary, the CS film has tightly connected internal molecules, leading to the high value of Young's modulus, which is difficult to deform.
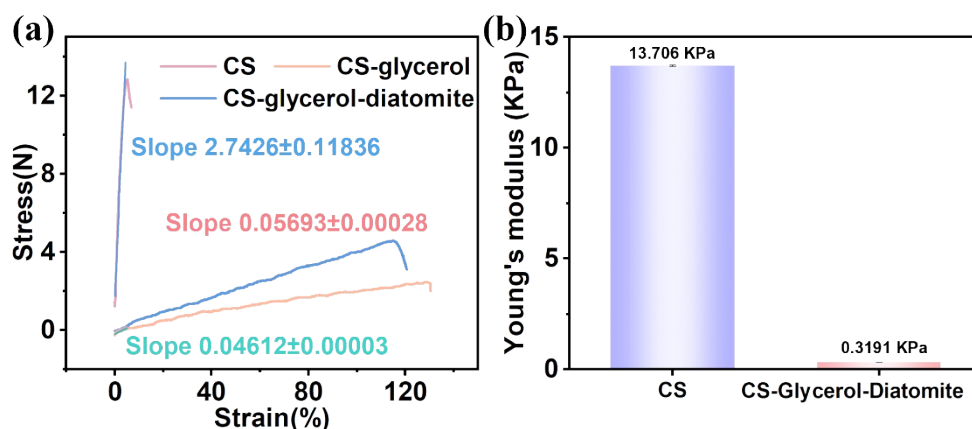
Figure S2 (a) Young's modulus of CS, CS–glycerol films and CS–glycerol–diatomite films, (b) Young's modulus error bars for CS and CS–glycerol–diatomite films.

4. Characterization of air permeability

The demonstration of the high air permeability of the composite film was done by comparing the water vapor transmission rate (WVTR) of the CS film and the composite film. Specific experiments were conducted by sealing the CS film and the composite film onto the top of a glass bottle containing distilled water, weighing the overall weight every 1 hour, and characterizing the WVTR by the difference in the overall weight. The characterization results are shown in Fig. S3, where the WVTR of the CS-glycerol-diatomite film is 1.6 times higher than that of the pure CS film, which suggests that the incorporation of glycerol and diatomite enhances the air permeability of the film.
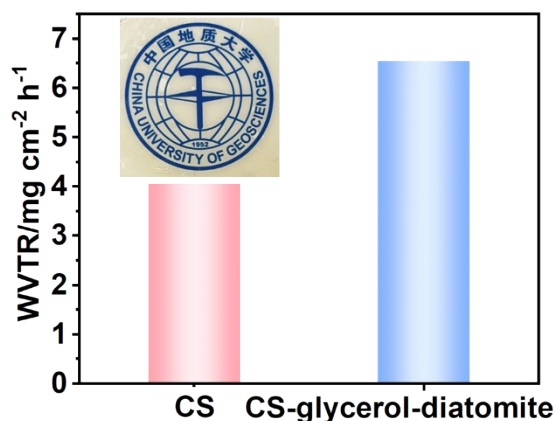

Figure S3 WVTR of CS film and CS-glycerol-diatomite film. The inset is an optical picture of CS-glycerol-diatomite film.

5. Working Mechanism

The mechanism of TENG was explained by the couple of contact electrification and electrostatic induction effects. Based on two friction materials' electron capture capabilities, the CS–glycerol-diatomite template composite film is positively charged, and FEP film is negatively charged with an equivalent charge magnitude (stage I). During the release from the counter film, the electric potential difference increases, resulting in electron transfer from the FEP film electrode to the CS–glycerol-diatomite composite film electrode (stage II). Electrons finished transferring after two dielectric films fully separated (stage III). In the contact process, the electrons moved from the
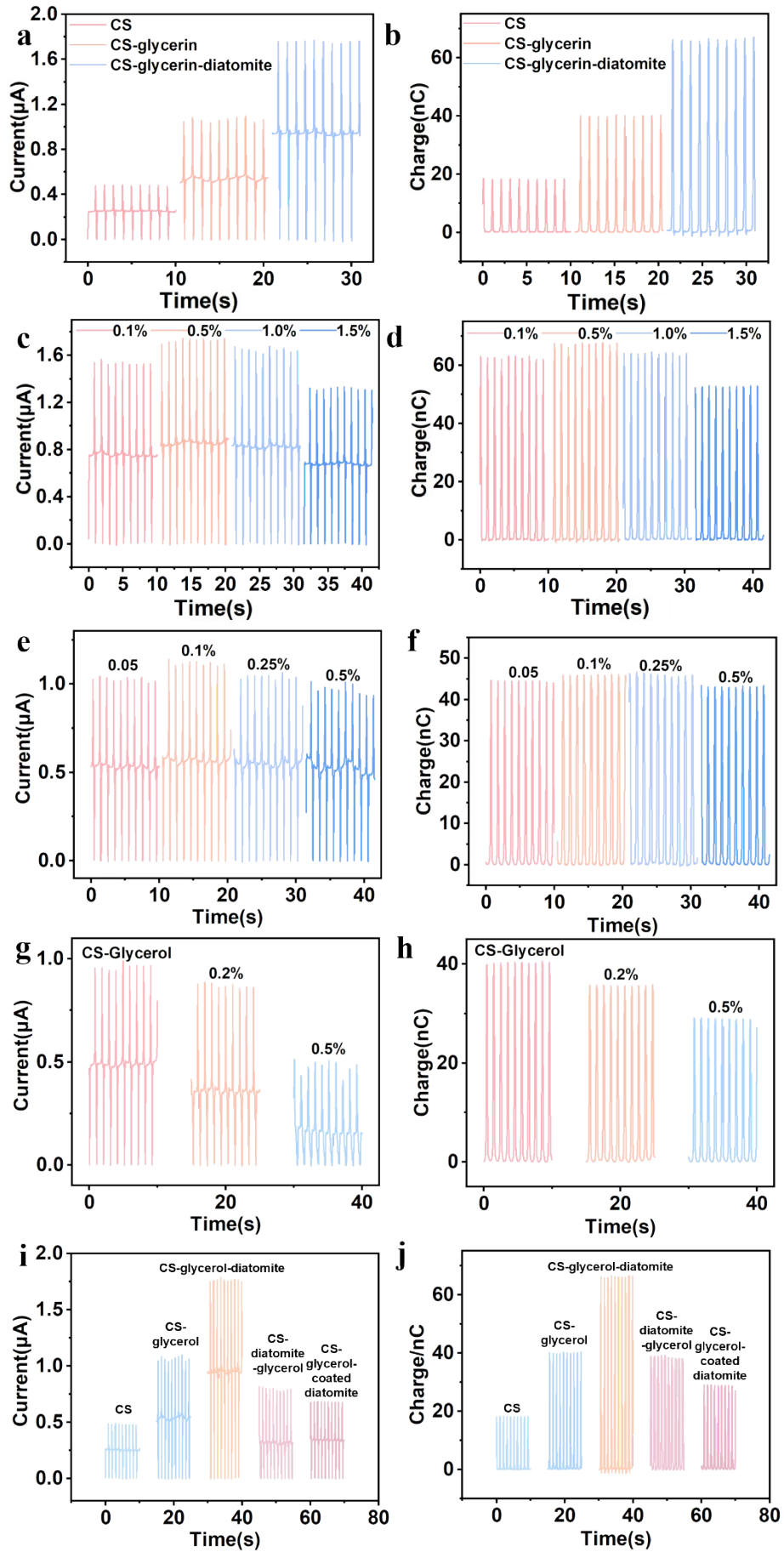
CS–glycerol-diatomite template composite film electrode to the FEP film electrode (stage IV). When the FEP film completely contacted with the CS–glycerol-diatomite template composite film, both electrodes change to the neutral charge state (stage I). The CS–glycerol-diatomite template composite film/FEP–based TENG can generate an electric current through this periodic process.
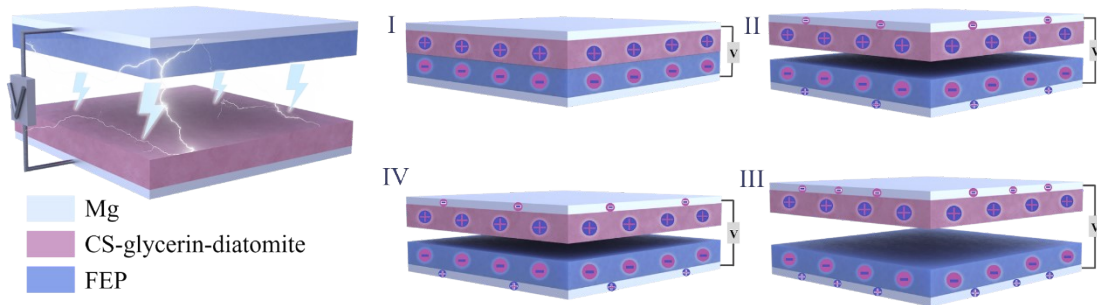
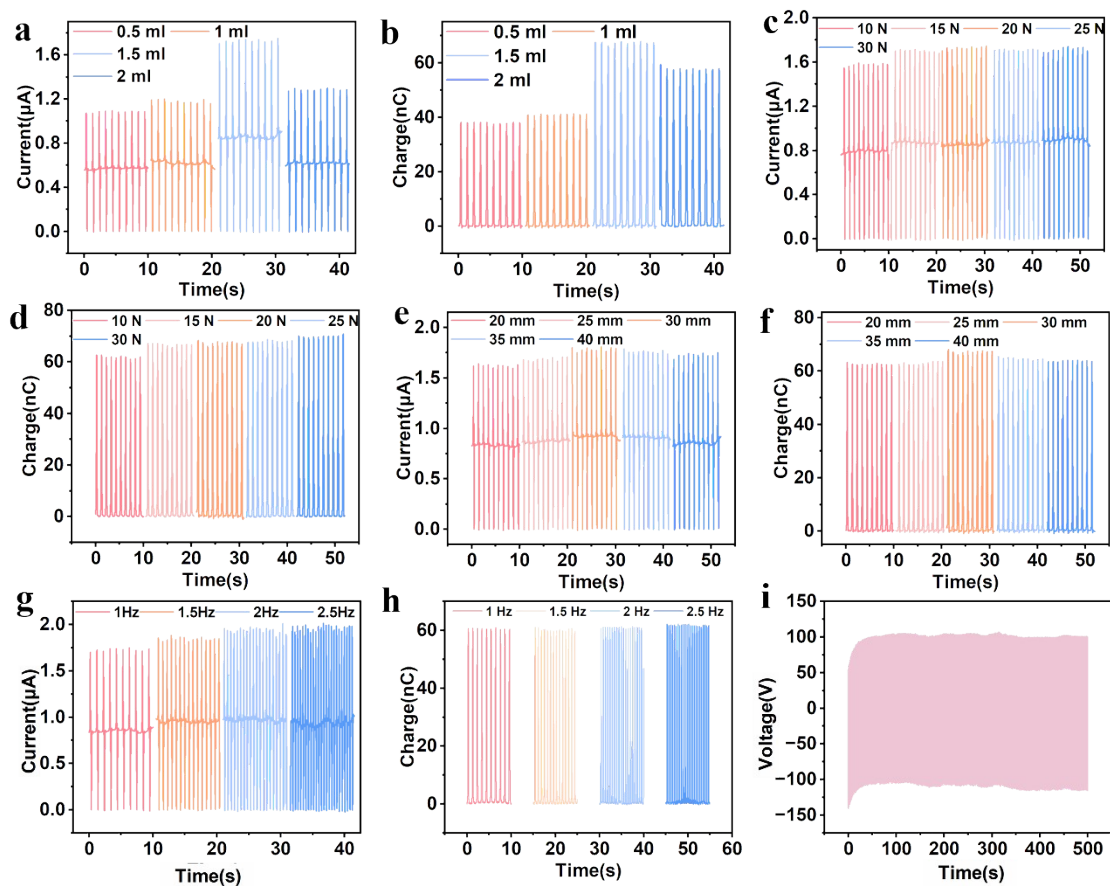Figure S4 The operating principle of the contact separation mode TENG.

6. Electrical output performance

Figure S5 Electrical output performance test of CS–glycerol–diatomite composite film–based TENG. (a) Short-circuit current at different diatomite contents. (b) Transferred charge at different diatomite contents. (c) Short-circuit current of CS-glycerol-diatomite composite film-based TENG. (d) Transferred charge of CS-glycerol-diatomite composite film-based TENG. (e) Short circuit of CS-diatomite-glycerol composite film-based TENG. (f) Transferred charge of CS-diatomite-glycerol composite film-based TENG. (g) Short circuit current of CS-glycerol-coated diatomite composite film-based TENG. (h) Transferred charge of CS-glycerol-coated diatomite composite film-based TENG. (i) Comparison of short circuit currents of CS films, CS-glycerol-diatomite films, CS-diatomite-glycerol films and CS-glycerol coated diatomite films. (j) Comparison of transferred charges of CS films, CS-glycerol-diatomite films, CS-diatomite-glycerol films and CS-glycerol coated diatomite films.

7. Short–circuit current and transfer of charge

Figure S6 Electrical output performance test of CS–glycerol–diatomite composite film–

based TENG. (a) Short circuit current under different glycerol contents. (b) Transferred charge under different glycerol contents. (c) Short circuit current under different applied forces. (d) Transferred charge under different applied forces. (e) Short circuit current at different separation distances. (f) Transferred charge at different separation distances. (g) Short circuit current under different frequencies. (h) Transferred charge under different frequencies. (i) Open circuit voltage during 0 seconds to 1000 seconds cyclic.
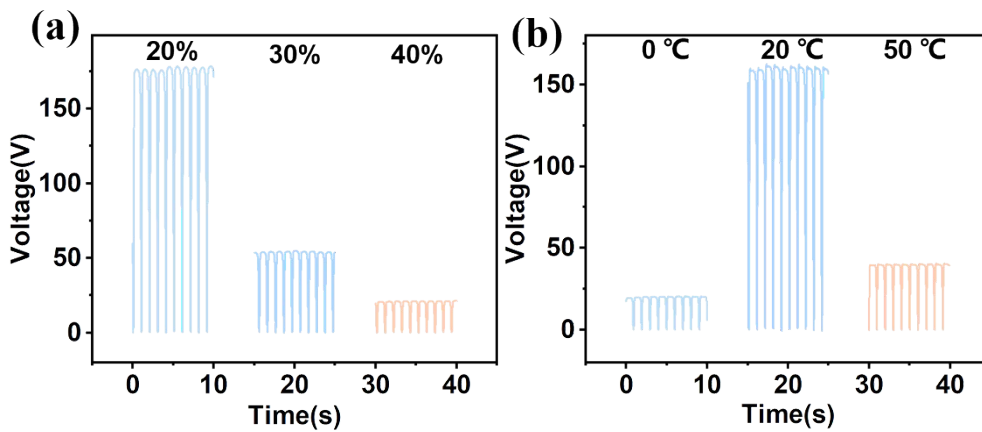
Figure S7 Output performance test of CS–glycerol–diatomite composite film–based TENG at different temperatures and humidity. (a) Output performance test of CS–glycerol–diatomite composite film–based TENG at different humidity. (b) Output performance test of CS–glycerol–diatomite composite film–based TENG at different temperatures.

8. COMSOL simulation

The modelling process assumes that the known physical quantities such as the electrical properties of the material (for example dielectric constant, conductivity) and the friction coefficient remain constant during the simulation. The physical quantities such as electric and magnetic fields at the boundary are uniform. The size of the friction layer is 20mm*20mm*5mm. The effect of temperature, humidity and other factors are not considered in the simulation process.
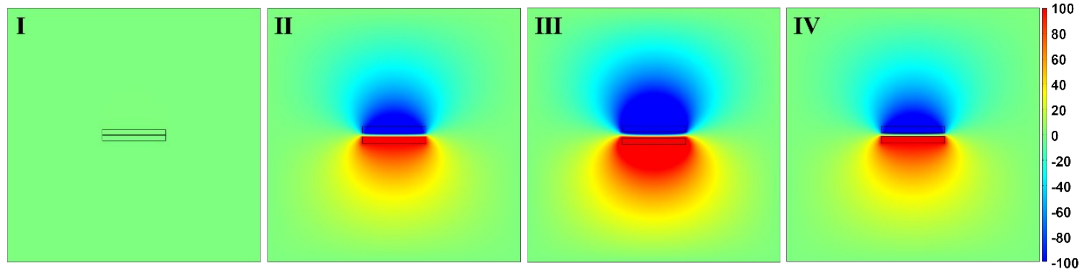
Figure S8 Theoretical model for the dielectric–to–dielectric contact–separation–mode TENG. (I) complete contact between friction layers, (II) Gradual separation between friction layers, (III) Complete separation between friction layers, (IV) Gradual contact between friction layers.

9. Calculation formula

The power density of TENG was calculated as Equation (1)

$$P = I^2R/A \tag{1}$$

where I is the output current for the corresponding resistance R, and A is the effective contact area.

Table S1 Detailed information such as the output performance of TENG composed of this material is compared with other materials in the field.

Friction layer	Electrode	Open-circuit voltage (V)	Short-circuit current (μA)	transfer charge (nC)	power density (μW cm^{-2})	Durability (cycles)	Ways to improve output performance	Application	Refs
Modified CFP coated with three layers of Ti$_{0.8}$O$_2$ NSs and five layers of Ag NPs, PDMS	Al	42	1	-	25	9300	The addition of conductive fillers produces conductive paths and promotes charge transport	Drives small electronics, harvesting energy human activity	[6]
CNF/PEI aerogel, PVDF nanofiber	Two aluminum strips	26	2.6	-	0.34 W m^{-2}	10000	Modifying CNF with PEI improves the power density	Detect human motion	[7]
Poly-ethyleneimine (PEI) paper, PTFE	Cu	68.6	4.47	9.12	_	900	Introduction of PEI improves the positive polarity of the friction layer	Self-powered pressure sensor	[8]
Amino silane modification of a CNF film, FEP	Conductive adhesive	155	17.5	-	0.22 W m^{-2}	10000	The positive electric property was improved by amino silane modification	_	[9]
Allicin grafted CNFs (Alc-S-CNF), PVDF	Al	7.9	5.13	2.76	10.13	7000	Allicin modification improves surface polarity and roughness	Energy harvesting devices	[10]
A-CNF film, FEP	Conductive adhesive	155	17.5	65	0.22 W m^{-2}	10000	Amino silane modification enhances the positive charge	Wearable electronics	[11]
Ethyl cellulose (EC)/PA6 nanofiber, PVDF/MXene	Cu	46	0.34	-	290 mW m^{-2}	14000	The introduction of MXene enhances the electronegativity	Self-powered sensor	[12]
Chitosan/BaTiO$_3$ nanorods, PTFE	Al	111.4	21.6	-	756	3000	The roughness is increased by adding BaTiO$_3$ filler	Large-scale power applications	[13]
BC/AgNWs/ BaTiO3, PDMS	Cu	87	7.1	35	75	3000	AgNWs and BaTiO$_3$ improve dielectric constant and roughness	Human–machine interaction device	[14]
BC/chitosan, PDMS/Cu	Cu	23	0.5	-	3.25 mW m^{-2}	1000	Cu nanoparticles improve electrical conductivity and contact area	Self-powered pressure sensors	[15]
Catechol-chitosan-diatom hydrogel, PDMS	Al	110	3.8	-	29.8	_	Adding diatoms increases the porosity	Wearable electronics	[16]
Chitosan/activated carbon composite,	Cu	48	—	-	12.208 mW	2000	AC to CS can enlarge the porosity,	Humidity\human motion	[17]

Materials	Electrode						Mechanism	Application	Ref.
FEP					m^{-2}		and reduce the resistance	sensor	
Carboxymethyl cellulose sodium (CMC-Na), CMC chitosan (CMCS)	Edible electrode	3	20	-	120 mW m^{-2}	3000	Nanofiber membrane prepared by electrospinning improve electric density	Power electronic equipment	[18]
CNF aerogel, PDMS	Ag	55.8	0.94	-	29 mW m^{-2}	50	The area of friction layer was enhanced by printing	Self-powered\ humidity sensor	[19]
Cellulose nanofibrils, FEP	ITO	32.8	35	-	_	_	The design of nanostructures increases the roughness	Triboelectric flooring\packag	[20]
Cellulose microfibers (CMFs), cellulose	Ag	21.9	0.17	-	7.68	_	Micro and nano structures increase the charge density	Self-powered healthcare	[21]
Chitosan-glycerol film, PTFE	Al	130	30	60	—	10000	The design of nanostructures increases the charge density	Wearable\self-powered sensors	[22]
Cellulose/PVA, hydrogel (CPH)	Cu	41	500 mA	15	_	4800	Preparation of hydrogel to enhance the friction layer area	Wearable electronic devices	[23]
MXene Ti$_3$C$_2$T$_x$/ CMC (MXene/CMC) aerogel	Cu	54.37	1.22	-	402.94 mW m^{-2}	1000	Porously 3D conductive network structure of aerogel increases the charge density	Self-powered sensor	[24]
Ag nanoparticles embedded with Ox-SWCNTs (Ag-Ox-SWCNT), (Ox-SWCNT/PVA/H$_3$PO$_4$) (Ox-SWCNT/PVA/H$_3$PO$_4$), PDMS	Ag	90	100	8	84.4 mW m^{-2}	10000	Carboxyl and hydroxyl group functionalized SWCNTs blended with PVA polymers to maintain conductive network	Self-charging power units, wearable Electronics	[25]
PWP (polyethylene oxide, water-polyurethane, phytic acid), low-temperature vulcanized (LTV) silicone rubber	Cu	197	17.3	10	2 W m^{-2}	10000	Sharp increase and rapid movement of mobile ions in PWP composites increase the output performance	Tactile sensor, epidermal input touchpad	[26]
VA-CaCl$_2$ film, silicone rubber	Al	165	55 mA	50	11.3 W m^{-2}	_	The addition of ions creates an internal ion polarization that increases the permittivity	_	[27]

| Material	Electrode	Voltage	Current	Charge	Power density	Durability	Mechanism	Application	Ref.
Polysiloxane-dimethylglyoxime-based polyurethane (PDPU)	AgNW bundle mesh	3.8	_	2.5	35 mW m^{-2}	10	The introduction of PDPU promotes charge transport	Self-powered sensing	[28]
Conductive polyurethane (C-PU) foam, PTFE	Al	102	2.2	-	1.5	_	The introduction of C-PU increases the contact area	_	[29]
Thermoplastic polyurethane (TPU), PTFE	C-AgNW ink layer	12.5	18.4	1.45	_	2000	Improve contact area through screen-printing process	Wireless wearable device, detection human motion	[30]
Silicon rubber (Ecoflex) films, PU foam	Cu	50	0.5	15	_	50000	Via changing the mesh grid and the foaming conditions	Self-powered sensing	[31]
PVA/Mxene nanofibers, Silk fibroin nanofibers	Cu	118.4	_	-	1087.6 mW m^{-2}	124000	The introduction of nanostructures increases the charge density	Monitoring body movement	[32]
PU, PFE	Cu	105.6	20.3	-	0.56 mW m^{-2}	10000	Aerogel film increases contact area	Biomechanical sensor	[33]
Auxetic PU foam, PTFE, Kraft paper	Cu	6.98	24.53 mA	80	_	50000	Kraft paper is used as a friction layer to enhance roughness	Wearable electronics device	[34]
CS-Glycerol-Diatomite, FEP	Mg	205	1.65	60	408 mW m^{-2}	10000	Plasticization and the introduction of hydrogen bonds combine to enhance output performance.	Waist-wearable respiration sensor	This work

10. Endogenous TENG

The working mechanism of endogenous TENG is mainly in the process of releasing pressure, when the pressure is released slowly, the upper friction layer will be released preferentially, so the friction macroscopic electric field generated by this friction layer can be applied to the structure of the following friction layer, which induces more charges, and when the pressure is continued to be released, the accumulated charges will be released through the action of the electric field to form an electric current, which enhances the output performance.
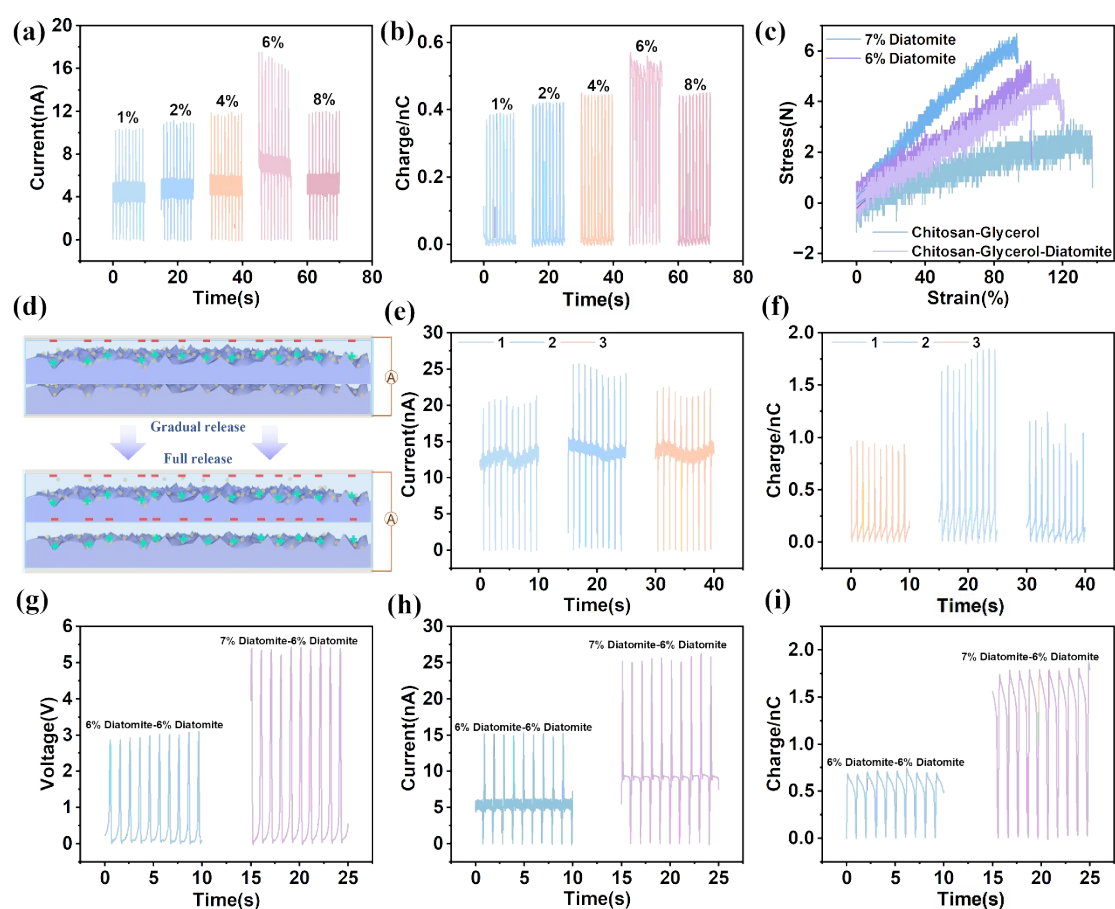
Figure S9 Output performance of endogenous TENG (a) Short circuit current under different diatomite contents. (b) Transferred charge under different diatomite contents. (c) Stress-strain curves of four composite films. (d) Schematic representation of the working mechanism of endogenous TENG from slow to complete release. (I) Schematic diagram of the working mechanism when the force is applied. (II) Schematic diagram of the working mechanism when the force is released. (e) Comparison of short circuit current for different layers of composite film. (f) Comparison of transferred

charge for different layers of composite film. (g) Open circuit voltage comparison of non-endogenous TENG and endogenous TENG. (h) Open circuit comparison of non-endogenous TENG and endogenous TENG. (i) Transferred charge comparison of non-endogenous TENG and endogenous TENG.
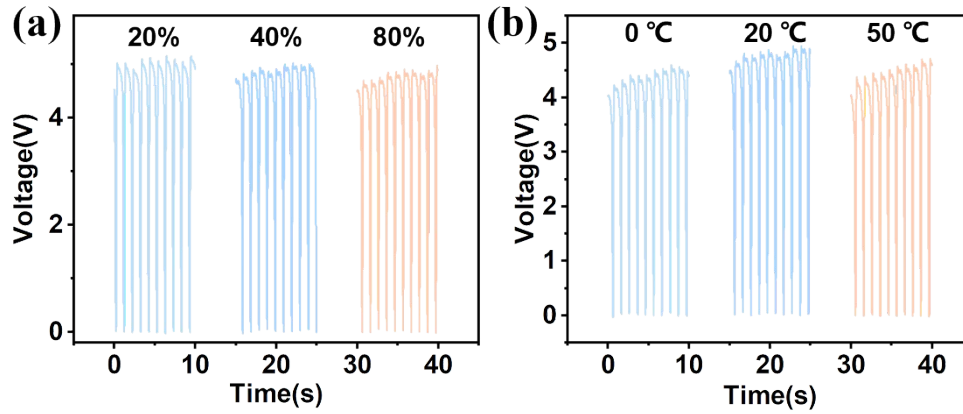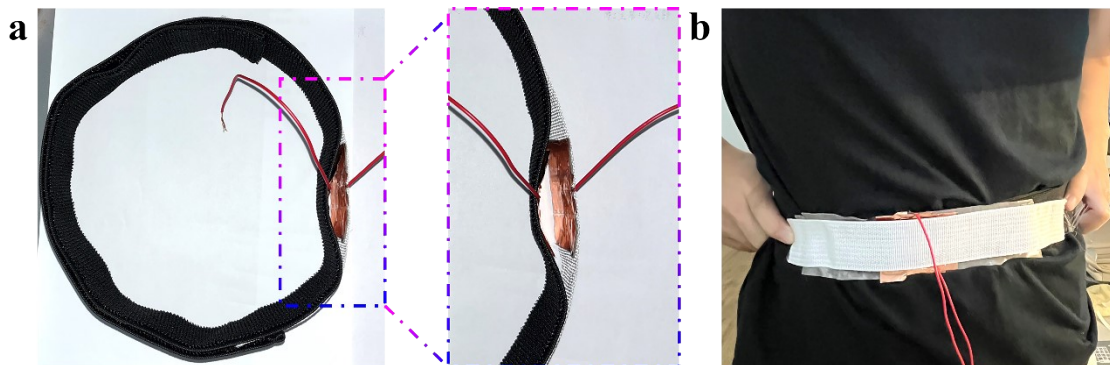

Figure S10 Output performance test of endogenous TENG at different temperatures and humidity. (a) Output performance test of endogenous TENG at different humidity. (b) Output performance test of endogenous TENG at different temperatures.

11. Information transfer sensors and waist-wearable respiration sensor
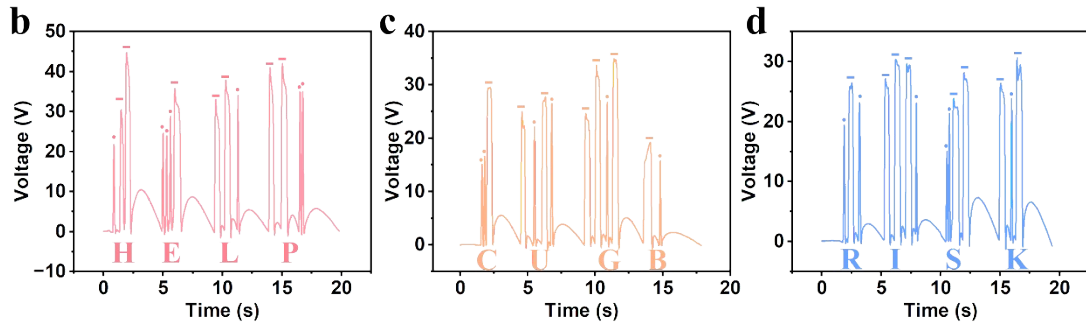

Figure S11 (a) Physical drawing and enlarged drawing of a waist-worn respiratory sensor. (b) Physical drawing of a waist-worn respiratory sensor in operation.
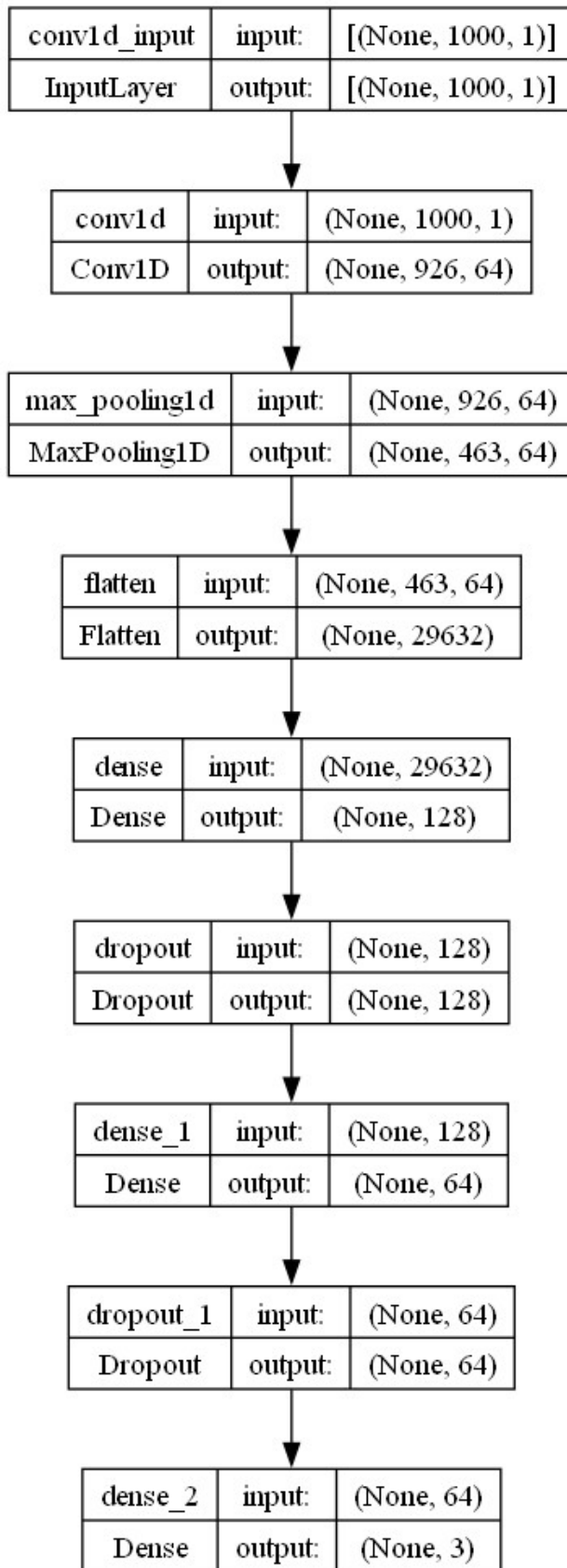
a A	B	C	D	E	F	G	H	I	J
·-	-·	···-	-··	···-	·--·	--·-	·--	---·	·-··
K	**L**	**M**	**N**	**O**	**P**	**Q**	**R**	**S**	**T**
-·-	--·	··-·	·-·	-·--	--··	·--	·-·	··--	·---
U	**V**	**W**	**X**	**Y**	**Z**				
-·-·	-··-	··	-···	--	····				

Figure S12 (a) The 26 letters Morse code. (b)Spelling "HELP". (c) Spelling of "CUGB". (d) Spelling "RISK".

12. Machine learning algorithms

We used three algorithms, CNN, SVM and KNN, for classification and compared the results and found that CNN has the best classification effect. In the training process of CNN, we divided 158 sets of samples based on all the collected data, and each set of samples contains 1000 time series points. The dataset includes three categories of fast, medium, and slow actions, with a number of samples under each category, and is divided into a training set and a test set in the ratio of 8:2.   As shown in Figure S11, the convolutional layer of this CNN structure uses 64 convolutional kernels, each with a size of 75 (kernel_size=75). The activation function of the convolutional layer is ReLU, and the input shape is (1000, 1), which indicates that each sample consists of a single-channel sequence of 1000 time points.   KNN and SVM process data differently from CNN. In KNN and SVM, instead of using the original sequence data directly, 14 features, including mean, variance, standard deviation, etc., are manually extracted from each set of 1000 points of data, and its used as inputs to KNN and SVM models for classification.

conv1d_input	input:	[(None, 1000, 1)]
InputLayer	output:	[(None, 1000, 1)]

conv1d	input:	(None, 1000, 1)
Conv1D	output:	(None, 926, 64)

max_pooling1d	input:	(None, 926, 64)
MaxPooling1D	output:	(None, 463, 64)

flatten	input:	(None, 463, 64)
Flatten	output:	(None, 29632)

dense	input:	(None, 29632)
Dense	output:	(None, 128)

dropout	input:	(None, 128)
Dropout	output:	(None, 128)

dense_1	input:	(None, 128)
Dense	output:	(None, 64)

dropout_1	input:	(None, 64)
Dropout	output:	(None, 64)

dense_2	input:	(None, 64)
Dense	output:	(None, 3)

1

2 Figure S13 Diagram of the structure of a CNN

3

Reference

1. B. Qian, X. Li, Y. Wang, J. Hou, J. Liu, S. Zou, F. An and W. Lu, *Advanced Materials*, 2024, DOI: 10.1002/adma.202310926.

2. Z. Hui, Z. Zhang, Y. Wang, R. Zhang, X. Liu, M. Jiang, F. Ju, W. Hou, Z. Xia, D. Wang, P. Wang, Y. Pei, R. Yan, Y. Zhang, Q. Chen, W. Huang and G. Sun, *Advanced Materials*, 2024, DOI: 10.1002/adma.202314163.

3. C. Ma, J. Su, B. Li, A. Herrmann, H. Zhang and K. Liu, *Advanced Materials*, 2020, DOI: 10.1002/adma.201907697.

4. C. Luo, Y. Chen, Z. Huang, M. Fu, W. Ou, T. Huang and K. Yue, *Advanced Functional Materials*, 2023, DOI: 10.1002/adfm.202304486.

5. Y. Li, D. Li, J. Wang, T. Ye, Q. Li, L. Li, R. Gao, Y. Wang, J. Ren, F. Li, J. Lu, E. He, Y. Jiao, L. Wang and Y. Zhang, *Advanced Functional Materials*, 2023, DOI: 10.1002/adfm.202310260.

6. S. Sriphan, T. Charoonsuk, T. Maluangnont, P. Pakawanit, C. Rojviriya and N. Vittayakorn, *ADVANCED MATERIALS TECHNOLOGIES*, 2020, **5**.

7. H.-Y. Mi, X. Jing, Q. Zheng, L. Fang, H.-X. Huang, L.-S. Turng and S. Gong, *NANO ENERGY*, 2018, **48**, 327-336.

8. W. Shihao, L. Gang, L. Wenxia, Y. Dehai, L. Guodong, L. Xiaona, S. Zhaoping, W. Huili and L. Hong, *Nano Energy*, 2021, DOI: 10.1016/j.nanoen.2021.106859.

9. C. Yao, X. Yin, Y. Yu, Z. Cai and X. Wang, *ADVANCED FUNCTIONAL MATERIALS*, 2017, **27**.

10. S. Roy, H.-U. Ko, P. K. Maji, L. Van Hai and J. Kim, *Chemical Engineering Journal*, 2019, DOI: 10.1016/j.cej.2019.123723.

11. S. Nie, C. Cai, X. Lin, C. Zhang, Y. Lu, J. Mo and S. Wang, *ACS Sustainable Chemistry & Engineering*, 2020, DOI: 10.1021/acssuschemeng.0c07531.

12. J. Huang, Y. Hao, M. Zhao, W. Li, F. Huang and Q. Wei, *ACS Applied Materials & Interfaces*, 2021, DOI: 10.1021/acsami.1c03894.

13. S. Pongampai, T. Charoonsuk, N. Pinpru, P. Pulphol, W. Vittayakorn, P. Pakawanit and N. Vittayakorn, *COMPOSITES PART B-ENGINEERING*, 2021, **208**.

14. Y. Hua, S. Yan, L. Chen, L. Yan, M. Hong-zhi, Z. Yu-hao, Y. Bo, S. Jia-bin and Y. Ming-bo, *Composites Part A: Applied Science and Manufacturing*, 2021, DOI: 10.1016/j.compositesa.2021.106646.

15. J. Huang, Y. Hao, M. Zhao, H. Qiao, F. Huang, D. Li and Q. Wei, *COMPOSITES PART A-APPLIED SCIENCE AND MANUFACTURING*, 2021, **146**.

16. J.-N. Kim, J. Lee, H. Lee and I.-K. Oh, *NANO ENERGY*, 2021, **82**.

17. Z. Xu, D. Zhang, X. Liu, Y. Yang, X. Wang and Q. Xue, *NANO ENERGY*, 2022, **94**.

18. K. Yan, X. Li, X.-X. Wang, M. Yu, Z. Fan, S. Ramakrishna, H. Hu and Y.-Z. Long, *Journal of Materials Chemistry A*, 2020, DOI: 10.1039/d0ta08909e.

19. C. Qian, L. Li, M. Gao, H. Yang, Z. Cai, B. Chen, Z. Xiang, Z. Zhang and Y. Song, *Nano Energy*, 2019, DOI: 10.1016/j.nanoen.2019.103885.

20. C. Yao, A. Hernandez, Y. Yu, Z. Cai and X. Wang, *NANO ENERGY*, 2016, **30**, 103-108.

21. X. He, H. Zou, Z. Geng, X. Wang, W. Ding, F. Hu, Y. Zi, C. Xu, S. L. Zhang, H. Yu, M. Xu, W. Zhang, C. Lu and Z. L. Wang, *Advanced Functional Materials*, 2018, DOI: 10.1002/adfm.201805540.

22. Y.-T. Jao, P.-K. Yang, C.-M. Chiu, Y.-J. Lin, S.-W. Chen, D. Choi and Z.-H. Lin, *NANO*

1   *ENERGY*, 2018, **50**, 513-520.

2 23.   Y. Wang, L. Zhang and A. Lu, *Journal of Materials Chemistry A*, 2020, DOI:
3   10.1039/d0ta02010a.

4 24.   Y. Cheng, W. Zhu, X. Lu and C. Wang, *Nano Energy*, 2022, DOI:
5   10.1016/j.nanoen.2022.107229.

6 25.   H. J. Yang, J.-W. Lee, S. H. Seo, B. Jeong, B. Lee, W. J. Do, J. H. Kim, J. Y. Cho, A. Jo, H. J.
7   Jeong, S. Y. Jeong, G.-H. Kim, G.-W. Lee, Y.-E. Shin, H. Ko, J. T. Han and J. H. Park, *Nano*
8   *Energy*, 2021, DOI: 10.1016/j.nanoen.2021.106083.

9 26.   Z. Bai, Y. Xu, C. Lee and J. Guo, *Advanced Functional Materials*, 2021, DOI:
10   10.1002/adfm.202104365.

11 27.   C. Jian Ye, K. Jason Soon Chye, C. Ruihao, A. Kean Chin, V. Thamil Selvi, C. Binghui, L. Jing,
12   F. Chuan Yi and G. Wee Chen, *Nano Energy*, 2021, DOI: 10.1016/j.nanoen.2021.106616.

13 28.   J. Xiong, G. Thangavel, J. Wang, X. Zhou and P. S. Lee, *Science Advances*, 2020, DOI:
14   10.1126/sciadv.abb4246.

15 29.   H. Zhang, Y. Lu, A. Ghaffarinejad and P. Basset, *Nano Energy*, 2018, DOI:
16   10.1016/j.nanoen.2018.06.038.

17 30.   G. Zhu, P. Ren, J. Yang, J. Hu, Z. Dai, H. Chen, Y. Li and Z. Li, *Nano Energy*, 2022, DOI:
18   10.1016/j.nanoen.2022.107327.

19 31.   X. Yibing, H. Jiashun, L. Heng, M. Hao-Yang, N. Gaolei, Z. Xiaoshuai, J. Xin, W. Yameng, Z.
20   Guoqiang, L. Chuntai and S. Changyu, *Nano Energy*, 2021, DOI:
21   10.1016/j.nanoen.2021.106827.

22 32.   C. Jiang, C. Wu, X. Li, Y. Yao, L. Lan, F. Zhao, Z. Ye, Y. Ying and J. Ping, *Nano Energy*, 2019,
23   DOI: 10.1016/j.nanoen.2019.02.052.

24 33.   Z. Saadatnia, S. G. Mosanenzadeh, T. Li, E. Esmailzadeh and H. E. Naguib, *Nano Energy*, 2019,
25   DOI: 10.1016/j.nanoen.2019.104019.

26 34.   Y. Feng, X. Huang, S. Liu, W. Guo, Y. Li and H. Wu, *Nano Energy*, 2019, DOI:
27   10.1016/j.nanoen.2019.05.043.

28